

# Multifunctional “Janus-Type” Bilayer Films Combine Broad-Range Tissue Adhesion with Guided Drug Release

Ceren Kimna, Maria G. Bauer, Theresa M. Lutz, Salma Mansi, Enes Akyuz, Zuleyha Doganyigit, Percin Karakol, Petra Mela, and Oliver Lieleg\*

Tissue healing is a challenging process that requires the successful and simultaneous management of conflicting priorities. While promoting wound closure, a battle must be won against different external factors that may adversely affect the healing process. Here this problem is approached by creating asymmetrically designed double-layer Janus-type bilayer films where distinct functions are implemented into the two sides of the film. Once deployed, those Janus-type films exhibit strong adhesion to a wide variety of wet tissues and canalize the release of integrated therapeutics toward the tissue side. At the same time, the outer surface of the films acts as a shield against tribological stress, pathogens, and cellular immune recognition. Moreover, when compared to untreated wounds, Janus-treated skin lesions show accelerated wound closure as well as fast formation of new, intact tissue. Having performed their tasks, Janus-type films degrade without leaving any traces on the tissues, which makes it possible to apply them to sensitive body surfaces. Thus, it is expected that the Janus-type bilayer films designed here can be used in a variety of medical applications where conflicting demands must be met at the same time.

*Stenocara gracilipes* employs a combination of both, hydrophilic and superhydrophobic areas on its head to efficiently collect water.<sup>[1]</sup> Similar to biological examples, also many problems in materials science benefit from the possibility to combine orthogonal properties into one and the same object. Macroscopically, this can be achieved relatively easily: for instance, the two opposing surfaces of a table tennis racket are designed to interact differently with the ball, e.g., to accelerate or slow down its motion. Microscopically, this is more difficult even though there are biomolecules such as lipids that combine antagonistic properties such as hydrophilic and hydrophobic regions. Nevertheless, the development of Janus-like objects was successful for selected applications such as separation processes, catalysis, electronic displays, and electrical/magnetic actuators.<sup>[2–4]</sup> Yet, in other areas, such as the management of wet tissue wounds, the


## 1. Introduction

There are several examples where nature has found a way to combine apparently contradicting properties into the same material to achieve a specific function. For instance, the desert beetle

simultaneous accomplishment of conflicting tasks remains a tremendous challenge: here, strong adhesion to the (wet) point-of-care is required while uncontrolled adhesion to neighboring tissues needs to be prevented.<sup>[5]</sup> These conflicting tasks are especially critical when wet-adhesive materials are applied to sensitive areas such as buccal, ocular, or intrainstestinal tissue.

C. Kimna, M. G. Bauer, T. M. Lutz, O. Lieleg  
School of Engineering and Design  
Department of Materials Engineering  
Technical University of Munich  
Boltzmannstraße 15, 85748 Garching, Germany  
E-mail: oliver.lieleg@tum.de

C. Kimna, M. G. Bauer, T. M. Lutz, O. Lieleg  
Center for Protein Assemblies (CPA)  
Technical University of Munich  
Ernst-Otto-Fischer Straße 8, 85748 Garching, Germany

 The ORCID identification number(s) for the author(s) of this article can be found under <https://doi.org/10.1002/adfm.202105721>.

© 2022 The Authors. Advanced Functional Materials published by Wiley-VCH GmbH. This is an open access article under the terms of the Creative Commons Attribution-NonCommercial License, which permits use, distribution and reproduction in any medium, provided the original work is properly cited and is not used for commercial purposes.

DOI: 10.1002/adfm.202105721

S. Mansi, P. Mela  
Medical Materials and Implants  
Department of Mechanical Engineering and Munich Institute of Biomedical Engineering  
TUM School of Engineering and Design  
Technical University of Munich  
Boltzmannstr. 15, 85748 Garching, Germany

E. Akyuz  
Faculty of Medicine  
Department of Biophysics  
University of Health Sciences  
Istanbul 34668, Turkey

Z. Doganyigit  
Faculty of Medicine  
Department of Histology and Embryology  
Yozgat Bozok University  
Yozgat 66900, Turkey

P. Karakol  
Sisli Hamidiye Etfal Research and Training Hospital  
Department of Plastic Reconstructive and Aesthetic Surgery  
University of Healthy Sciences  
Istanbul 34371, Turkey

In the field of wound management, asymmetric functionality often goes beyond macromechanical aspects: although good microscopic interaction of a material with proteins is required for good tissue adhesion, this property is undesired on the other side facing away from the tissue: there, protein-based conditioning films often trigger cellular biofouling events and can provoke unfavorable immune responses.<sup>[6]</sup> Similarly, drug transport from the therapeutic material to the wound site is required to promote the healing process; however, the diffusive liberation of drugs into surrounding body fluids (e.g., blood, mucus, and interstitial fluids) would strongly reduce the efficiency of the treatment and could cause unwanted side effects.

To date, many different adhesive formulations—mostly in the form of hydrogels—have been introduced to achieve better mechanical properties than those provided by commercial adhesives used in clinical applications.<sup>[7–12]</sup> To tackle the problems associated with using surgical sutures (e.g., requiring expert skills and a suture removal appointment), very promising materials with strong adhesion properties were developed in the last years. Recent examples include a polyethylenimine-poly(acrylic acid) powder for closing gastrointestinal perforations,<sup>[13]</sup> poly(vinyl alcohol)-dihydroxyphenylalanine (DOPA) films for the delivery of drugs to wet buccal tissue,<sup>[14]</sup> and macroporous carboxymethyl/agarose hydrogels for the delivery of Ag<sup>+</sup> ions.<sup>[15]</sup> These materials all exhibit strong tissue adhesion in combination with promising biological performance. Furthermore, materials for wet tissue adhesion can be equipped with important additional features such as controlled cell engraftment,<sup>[16,17]</sup> self-healing,<sup>[18,19]</sup> and hemorrhage control.<sup>[20,21]</sup> However, one clinical problem that remains is the postsurgical adhesion of such materials to other, undesired tissue areas.

To cope with this problem, medical materials with asymmetric functionalities were recently introduced, and they were indeed successful in promoting tissue repair *in vivo*.<sup>[22–25]</sup> For example, Cui et al.<sup>[22]</sup> presented a Janus structure with oppositely charged surfaces, which enables the overall material to seal tissue perforations and—at the same time—prevents undesired adhesions to its exterior part. Very recently, a three-layered Janus adhesive with asymmetric wetting properties developed by Xu et al.<sup>[23]</sup> was found to be successful in keeping the wound area dry while absorbing the wound exudate. Other very recent and highly promising examples from this area are peritoneum-inspired porous poly(vinyl alcohol) (PVA) hydrogels for canalizing cellular growth at the desired site,<sup>[26]</sup> and double-layered (ionically and covalently cross-linked) alginate/chitosan films for advanced tendon healing.<sup>[25]</sup> These asymmetric materials provide a set of distinct functions for the wound-healthy tissue interface. However, these materials exhibit a long lifetime, which limits their use to specific applications that are strictly controlled under medical care. Thus, multifunctional “all-in-one” solutions that synergistically manage different, and—indeed—often somewhat conflicting tasks, that are easy to use and rapidly make way for new, healed tissue by decomposing autonomously are scarce.

Here, we present asymmetrically designed Janus-type bilayer films to address all the problems listed above simultaneously. These bilayer films were engineered such that they provide distinct functionalities on their opposing surfaces to fulfill multiple tasks relevant for the treatment of epithelial wounds

(Figure 1a). The bilayer material combines a sticky, hydrogel-forming bottom layer based on dopamine-conjugated hyaluronic acid with a lubricating, nonadhesive top layer based on mucin glycoproteins. Materials comprising multifunctional mucins were introduced earlier, e.g., as anti-biofouling coatings, smart drug delivery materials, selective filters, and lubricating agents.<sup>[27]</sup> In our Janus-type bilayer films, the mucin-containing surface can protect the wet wound tissue of interest from biological and mechanical challenges such as nonspecific protein adsorption, bacterial colonization, and undesired tissue adhesions. The sticky layer, on the other hand, provides strong adhesion to various types of tissues (e.g., eye, tongue, intestine, and cartilage) and releases incorporated therapeutics into the desired direction only. Overall, they are easy to handle and can be effortlessly applied onto complex surfaces without requiring a supporting material for fixation. Furthermore, the Janus-type films readily adhere to wounds and accelerate the tissue regeneration process *in vivo* without causing any unwanted reactions. Finally, when their tasks are completed, the Janus-type bilayer films decompose on the applied surface and neither leave any traces nor induce alterations on the tissue microtopography. Thus, they do not require any professional (removal) step.

## 2. Results and Discussion

We here develop a hybrid material based on two layers with distinct functionalities: the bottom layer comprises dopamine conjugated hyaluronic acid (d-HA) biopolymers. This modified biomacromolecule was selected for two reasons: first, hyaluronic acid (HA) is known to condition intracellular signals responsible for cell proliferation and migration thus promoting wound healing;<sup>[28]</sup> second, catechol-type molecules can engage in unspecific, noncovalent interactions that enable adhesion to a broad range of materials including wet tissues.<sup>[29,30]</sup> Here, the successful conjugation of HA with dopamine is verified spectroscopically (Figure 1b), and the conjugation efficiency is calculated as 27%.

To ensure that adhesive properties are only present on one side of the film, the d-HA layer is coated with a nonadhesive polymer mesh. As a coating material, we select a PVA/mucin mixture which is electrospun onto the adhesive d-HA layer (Figure 1c,d). This mixture is chosen since PVA can be easily processed into fibers, thus serving as a structural reinforcement. Mucin glycoproteins are incorporated since mucin coatings have been shown to suppress biofouling events.<sup>[31]</sup> In fact, mucin-rich biomass obtained from different sources such as jellyfish and snails have been previously included in polymer mixtures to fabricate wound dressing materials.<sup>[32,33]</sup> Here, we purify porcine gastric mucins to obtain a well-defined macromolecular component for our bilayer film to harness the rich chemistry of mucins<sup>[34]</sup> as well as their important biological features such as prokaryotic and eukaryotic cell repellence<sup>[31,35,36]</sup> and immunomodulation ability.<sup>[37]</sup> In detail, when integrated into a nanofibrous network, we expect the mucins to establish two beneficial effects: first, due to the bacteria-repellent properties of mucins, their presence should protect epithelial cells covered with the bilayer film from infection; second, they can

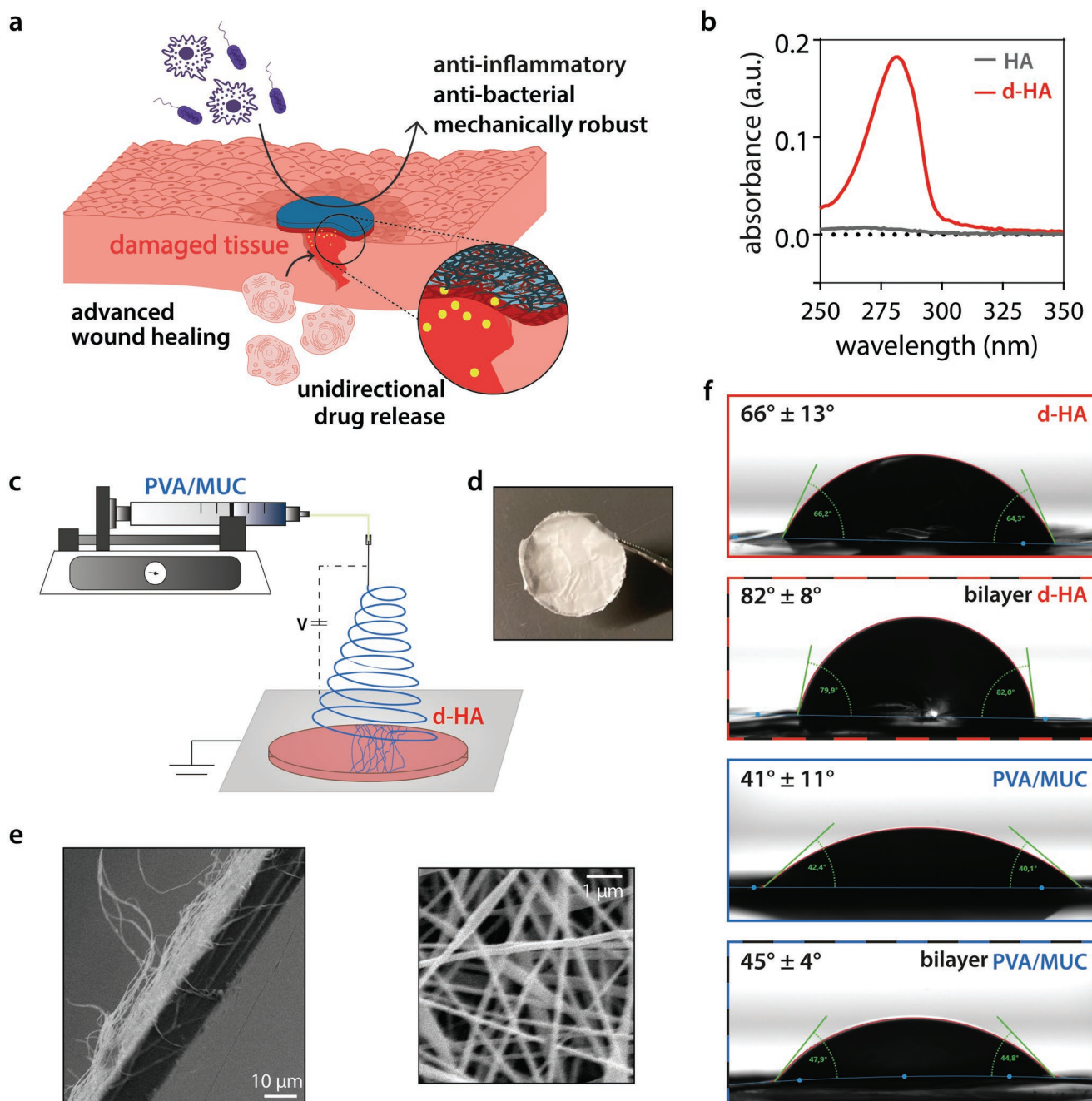


**Figure 1.** Production process and morphology of Janus-type bilayer films. a) Schematic representation of the multifunctional properties of the Janus-type bilayer films. b) Absorbance spectra of HA and -HA, respectively. The peak at 280 nm indicates successful catechol functionalization of HA as expected for d-HA. c) Schematic representation of the bilayer film formation procedure. d) Photograph of the top side of the bilayer film. e) A cross-sectional SEM image of the bilayer film (left) visualizes the nanofibers covering the top surface (right). f) Wettability of monolayers and each surface of the bilayer film. The value at the upper left corner of each photograph represents the contact angle calculated from  $n = 10$  independent samples.

help avoiding inflammatory reactions.<sup>[37]</sup> The fibers located in the top-layer of this two-component film have a random orientation and create a network with sub-micrometer mesh sizes in the range of  $(480 \pm 200)$  nm (Figure 1e; Figure S1, Supporting Information). Furthermore, a quantitative analysis of the surface roughness of the film demonstrates a homogeneous topography devoid of irregular bead formation (Figure S1, Supporting Information).

Another advantage brought about by the bilayer structure of the film is an improvement in mechanical properties. A film fabricated from d-HA alone exhibits a rather low stretching resistance ( $\approx 2$ -fold lower rupture forces compared to the bilayer film, Figure 2a,b) and weak overall integrity: the ensuing hydration of the biopolymer layer triggers rapid swelling, which turns this d-HA layer into a viscoelastic gel (Figure S2, Supporting Information). This can complicate the applicability of

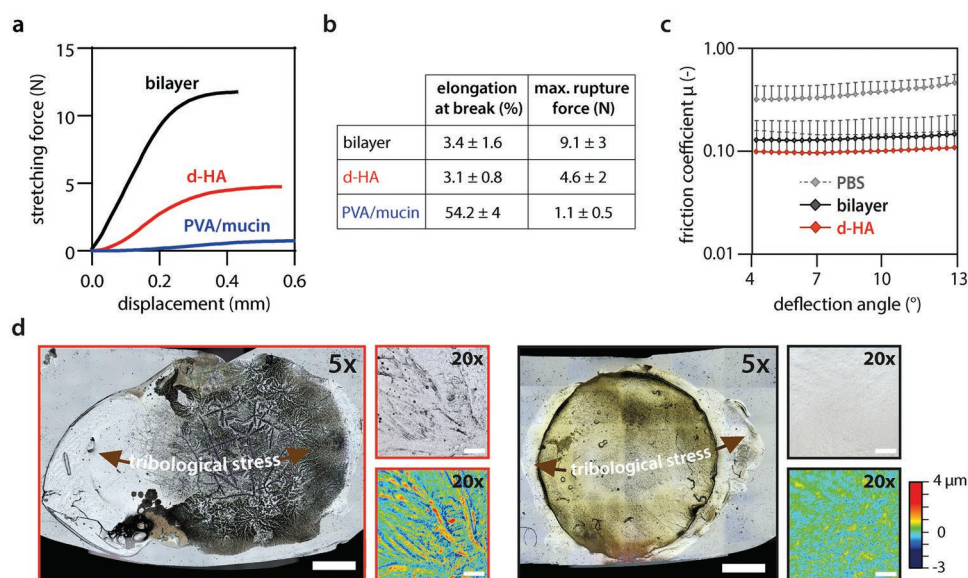


**Figure 2.** Mechanical properties of bilayer films. a) Representative stretching force–displacement curves of monolayer (d-HA and PVA/mucin, respectively) and bilayer films and b) the corresponding mechanical properties. c) Friction response and d) morphology of d-HA monolayers (left) and bilayer films (right) upon exposure to tribological stress. Images in gray scales represent combined laser confocal/light microscopy pictures; colored images represent topographical images (the color code on the right applies to both). Scale bars in 5 $\times$  images depict 2 mm and scale bars in 20 $\times$  images depict 0.1 mm. Data shown represent mean values, error bars denote the standard deviation as obtained from  $n \geq 3$  independent samples.

the film in a physiological setting. Yet, with the fibrous mucin/PVA layer added and cross-linked to the d-HA layer via glutaraldehyde vapor exposure, this issue is remedied. Furthermore, measurements performed with bilayer samples that contain monolayer extensions at either end showed that the bonding strength between the two layers of the film is higher than the tensile strength of individual monolayers (Figure S7, Supporting Information); thus, the integrity of the bilayer film under mechanical load should be sufficient for the application envisioned here. Similar to the results of the stretching tests, we also find enhanced robustness of the bilayer film toward tribological stress: when probed in an oscillatory tribology setup, both films show good friction behavior with low friction coefficients around  $\mu = 0.1$  (Figure 2c). This result was expected as both, HA and mucins, are highly hydrated macromolecules and thus enable hydration lubrication.<sup>[38,39]</sup> However, when both film variants are optically evaluated after the tribological test, clear differences are detected (Figure 2d): d-HA monolayers are spread out by  $(43 \pm 8)\%$ , whereas the bilayer films keep their circular shape and show only little spreading of  $(10 \pm 8)\%$  (Table S1, Supporting Information). Moreover, topographical images (Figure 2d, small images) indicate that the bilayer films maintain their homogenous surface structure even after tribological treatment; by contrast, d-HA monolayers exhibit wrinkles on their surface which indicates irreversible mechanical deformation. Owing to the added top layer, the film construct becomes sturdier and can be handled very well; it can be manually stretched (e.g., with a tweezer) and conveniently placed onto a complex surface such as a tongue or buccal mucosa (Video S1, Supporting Information) without being damaged.

In its dry state, the bilayer construct behaves as a thin, flexible film; upon contact with a wet surface, the bottom layer becomes a sticky, soft hydrogel. Importantly, we also selected hydrophilic

polymers for creating the nonadhesive top layer of the bilayer film.<sup>[31,40]</sup> Also, the surface of this nonadhesive side has hydrophilic properties; here, we measure contact angles of  $(41 \pm 11)^{\circ}$  (Figure 1f). Such a hydrophilic, well-hydrated film is well suited to keep a covered tissue layer moist and to prevent crust formation (e.g., when placed onto wounded tissues). To fulfill its function, the bilayer film should maintain its structural integrity until its main task, i.e., releasing the incorporated drugs while allowing for closure of damaged tissue, is completed. However, the material is not designed to remain on tissues for extended time periods: instead, the sticky, drug-loaded layer is engineered such that it degrades over a finite lifetime to be helpful for achieving the efficient release of its payload. Accordingly, in the next step, we spectrophotometrically determine the degradation profiles of each layer of the bilayer film (Figure 3a).

For those degradation tests, we incubate the bilayer film in different physiologically relevant fluids (i.e., phosphate-buffered saline (PBS), simulated tear fluid (STF), human saliva mimetic (HSM), and simulated intestinal fluid (SIF)); those fluids are selected to mimic the different liquid environments the film can encounter when placed onto a wet tissue in the human body. In all those tested conditions, the d-HA layer disintegrates more quickly, i.e., it reaches the maximum of its degradation profile within  $\approx 12$  h; by contrast, the mucin/PVA layer reaches its degradation peak after  $\approx 2$  days. From an application point of view, this delayed degradation behavior of the fibrous layer is very helpful: its presence protects the drug-loaded, sticky layer from undesired mechanical challenges and facilitates a controlled removal of the film once its task is completed. It is noteworthy to mention that, since the material developed here is mainly composed of biological polymers, their degradation products can be expected to be nontoxic. Additionally, it was shown that, owing to its high flexibility, PVA can be excreted through the

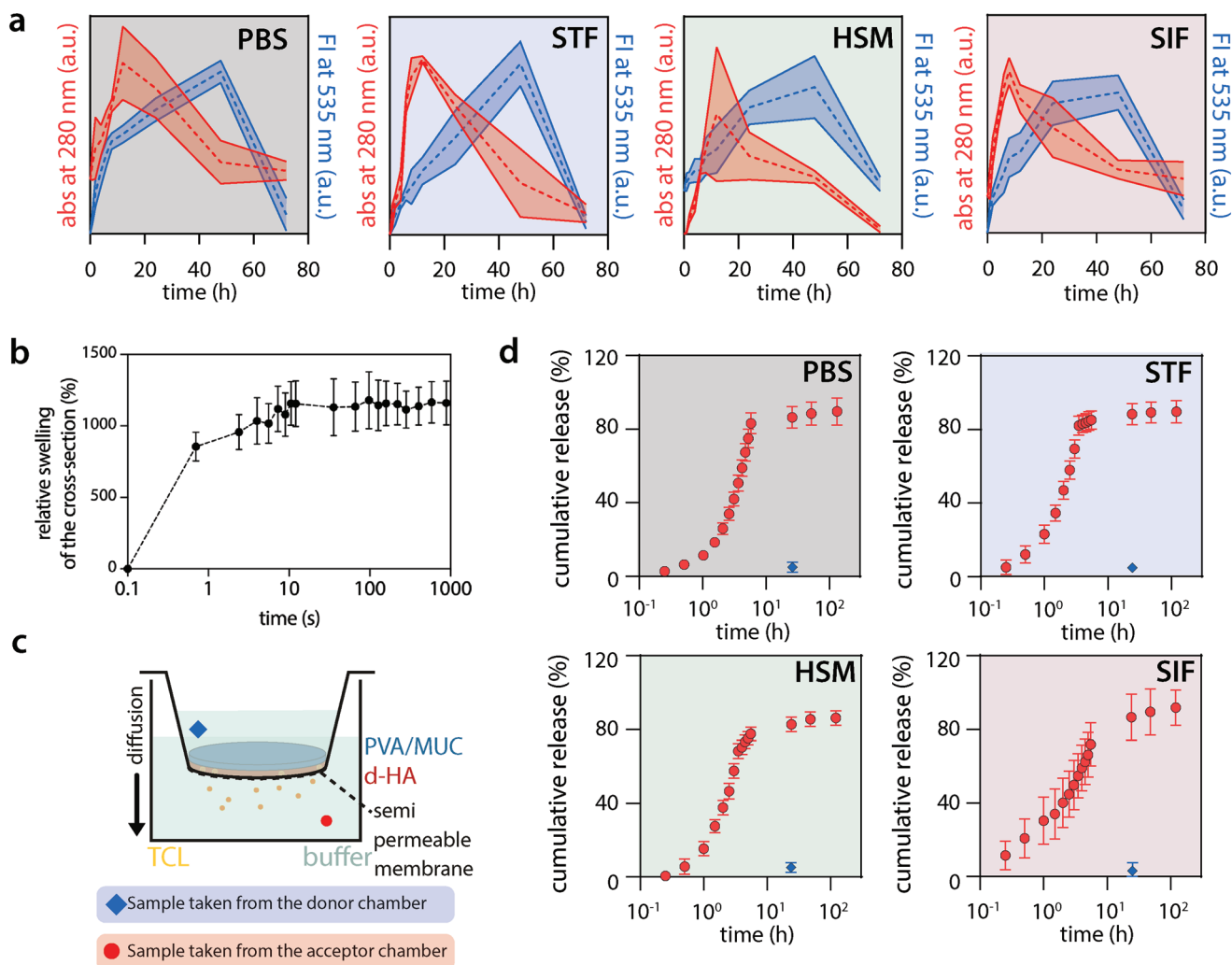


**Figure 3.** Degradation and drug release profiles of bilayer films. a) Degradation profiles of the two individual film layers when placed into physiologically relevant aqueous solutions (i.e., PBS, STF, HSM, and SIF, respectively). Blue and red lines correspond to PVA/mucin and d-HA layers, respectively. b) Relative swelling profile of the cross-section of the bilayer films ( $n = 7$ ). The error bars denote the standard error of the mean. c) Schematic representation of the experimental setup used for determining in vitro drug release profiles. d) Cumulative drug release from bilayer films immersed in PBS, STF, HSM, and SIF, respectively. Diamond symbols (blue) denote the percentage of drug released into the donor chamber after 24 h. Data shown represents mean values, error zones denote the standard deviation as obtained from  $n = 5$  independent samples.

kidneys without causing any damage to renal glomeruli;<sup>[41–44]</sup> moreover, PVA does not permanently accumulate in body tissues and it does not cause any toxic effects to cells.<sup>[45,46]</sup> Thus, the rapid and complete degradation behavior of the bilayer film construct under biological conditions is expected to be non-harmful to the body.

Next, the swelling profile of the bilayer films is determined by measuring the relative increase in their cross-sectional area. As shown in Figure 3b, the bilayer films start to swell rapidly after they get in contact with water. The swelling profile reaches a plateau level at  $\approx 1100\%$  after  $\approx 10$  s. This finding agrees very well with the strong hygroscopic nature of hyaluronic acid reported in the literature.<sup>[47]</sup> The fast and strong swelling behavior we here obtain for the bilayer films can also be beneficial when the material is applied to wounds: here, the film can immediately soak up the wound exudate, which otherwise can promote bacterial infection and thus hamper the wound healing process.<sup>[48]</sup>

The efficiency of the main task, i.e., guided (= unidirectional), the diffusive release of drugs toward the “tissue” side, is assessed in the next set of experiments. Here, we load the adhesive layer of the film with a model broad-spectrum antibiotic (tetracycline hydrochloride, TCL) and conduct drug release tests (Figure 3c). For all the model fluids the bilayer films are tested with, a highly efficient ( $>87\%$ ) and unidirectional drug liberation toward the attached surface is achieved. In detail, the drug release profiles enter a plateau around  $\approx 6$  h, and the release process is completed within 24 h. This result is consistent with the degradation profiles of the drug-containing d-HA layer of the film. Importantly, only a minor portion of the loaded drug ( $<8\%$ , diamond symbols in Figure 3d) is detected in the upper surface of the bilayer film. Thus, in a potential application, the fibrous surface not only provides mechanical stability but also acts as a gatekeeper during the therapeutic action by preventing a dilution of the incorporated drug molecules. Furthermore,

control experiments where the PVA/mucin layer was facing the semipermeable membrane showed that drug leakage to this side was minimal (<2% for the first 6 h), and the cumulative drug release after 3 days of incubation (when film degradation has already started to set in) was  $(13 \pm 8)$  % only (Figure S3, Supporting Information).

When a wound dressing material is placed onto a damaged tissue, protein adsorption onto the surface of the material can strongly affect its fate: whereas such adsorption of proteins from wound exudates can be beneficial for cellular adhesion (which improves the performance of such dressings<sup>[49]</sup>), nonspecific

protein adsorption may initiate an immune response by activating immune cells.<sup>[50]</sup> To investigate such unspecific protein-material interactions, we expose both sides of the bilayer film to fluorescently labeled bovine serum albumin (BSA, which is selected as a model protein since albumin is the most abundant protein in blood<sup>[51]</sup>) and quantify the fraction of protein adsorbed on either side of the film. In full agreement with the asymmetric properties of the bilayer film, we observe that the two sides of the construct exhibit significantly different BSA adsorption characteristics (Figure 4a). Whereas the d-HA-based layer binds  $\approx 25\%$  of the offered BSA molecules, only  $\approx 16\%$  of

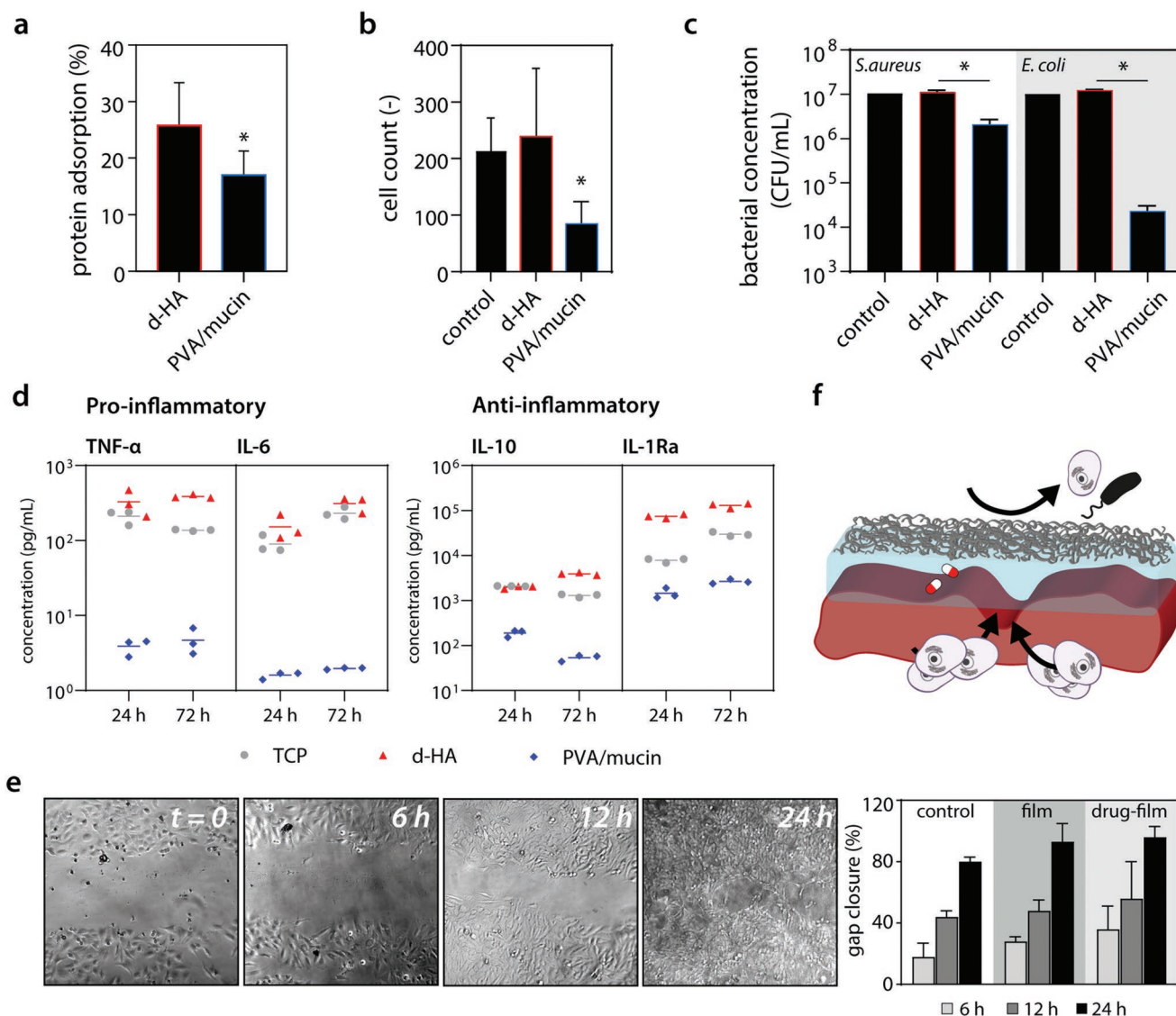


**Figure 4.** Interaction of proteins, prokaryotic, and eukaryotic cells with the bilayer films. a) Protein adsorption onto d-HA and PVA/mucin layers. An unpaired *t*-test was used to detect the statistical significances between the groups. b) HeLa cells counted after cultivation on the two different layers of the Janus-type film. c) *S. aureus* and *E. coli* adhesion to the d-HA and PVA/mucin surfaces of the bilayer film. For data shown in (b) and (c), a Welch's *t*-test was conducted to compare each group with the control. d) Cytokine expression levels in monocyte-derived macrophages after cultivation on tissue culture polystyrene (TCP, gray), d-HA layers (red), and PVA/mucin layers (blue). The data points denote the cytokine concentration per well, the vertical lines denote the average. e) Time-lapse microscopy images of HeLa cells covered with a bilayer film (left). The closure of the gap (right) was calculated as the average determined from  $n = 5$  independent samples per each group (right). f) Schematic representation of the distinct biological functions installed into the two surfaces of the bilayer film. Data in (a–d) represent mean values, and error bars denote the standard deviation as obtained from  $n = 5$  independent samples. Asterisks mark statistically significant differences based on a *p*-value of 0.05.

the BSA feed adsorb to the PVA/mucin layer. We speculate that this reduced amount of unspecific protein adsorption is probably brought about by the presence of mucins.<sup>[31]</sup>

Motivated by the outcome of the protein adsorption test, we next quantify cellular attachment to either side of the bilayer film using epithelial HeLa cells as a model cell line. As an in vivo application of the bilayer film has epithelial tissues as one likely target (see the wound healing tests described below), selecting an epithelial cell line for cytotoxicity and attachment tests was a natural choice.

As fluorescent images obtained after live/dead staining show (Figure S4a, Supporting Information), none of the two sides of the bilayer film elicits a perceivable cytotoxic effect—and neither do degradation products generated from the bilayer film (Figure S4b, Supporting Information). In terms of cell colonization efficiency, the d-HA surface of the bilayer film exhibits a similar density of adherent cells as the control, i.e., the wells of cell culture plates (Figure 4b). By contrast, we detect a significantly lower number of cells on the PVA/mucin surface. Additionally, the few adherent cells attached to this side of the bilayer film tend to show a round morphology, which suggests that they are only weakly attached. This observation agrees with previous findings that attributed a good cell-repellency of mucin-coated surfaces to a high density of strongly hydrated glycans provided by the mucin glycoproteins.<sup>[52–54]</sup> Thus, the mucin-containing top layer of the film can contribute to the protection of a wounded tissue area from uncontrolled cellular overgrowth. Moreover, we hypothesize that the presence of cysteines located in the polypeptide backbone of mucins might promote binding of collagen digesting enzymes (e.g., neutrophil elastase or metalloproteinases) thus potentially influencing the propensity of the bilayer film to become prematurely degraded by enzymatic attack.<sup>[55]</sup>

Although HA coatings have been shown to contribute to bacterial inhibition at the early stages,<sup>[56,57]</sup> the dopamine conjugation is likely to counter this effect. Indeed, both, *Staphylococcus aureus* and *Escherichia coli* bacteria adhere equally well to d-HA films as to control surfaces (Figure 4c). From an application point of view, this can be advantageous as it suggests that the bilayer films might also adhere well to infected wounds. In contrast, the PVA/mucin side significantly reduces bacterial adhesion. This effect is moderate for *S. aureus* but strong for *E. coli*. This is an important finding as bacterial colonization of the film (and subsequent biofilm formation) could drastically complicate wound treatment. Here, the PVA/mucin layer reduces such risks and can protect both the wound and bottom layer by repelling bacteria.

However, also in the absence of bacterial colonization, any artificial object may trigger a foreign body response by its interaction with immune cells. If this were to occur, the ensuing inflammation reaction would slow down the healing process. To evaluate a key aspect of the cellular immune response toward each surface of the bilayer film, the secretion of typical pro- and anti-inflammatory cytokines by macrophages incubated with either layer of the construct is assessed. As the results demonstrate (Figure 4d), also here, the asymmetric design of the bilayer film becomes evident: when seeded onto the d-HA layer, macrophages produce proinflammatory markers (expression of tumor necrosis factor- $\alpha$ /TNF- $\alpha$  and interleukin-6/IL-6) at similar levels as when directly seeded onto tissue culture plates (TCP). Furthermore, anti-inflammatory cytokines—particularly

the interleukin-1 receptor antagonist (IL-1Ra)—are expressed more strongly on d-HA than on TCP. This observation can be explained by previous findings, which reported hyaluronic acid-rich materials to promote the transformation of macrophages from a proinflammatory (M1) to a reparative (M2) phenotype.<sup>[58–60]</sup> When the macrophages are incubated on the PVA/mucin layer, we find remarkably low cytokine expression levels that are up to two orders of magnitude smaller than those obtained on both, TCP and d-HA surfaces. This outcome is in line with previous results on the short- and long-term response of macrophages seeded onto mucin-based materials: there, mucin-based gels were shown to have a broad dampening effect on the cytokine expression in macrophages, both in vitro and in vivo.<sup>[37,61]</sup> Thus, the upper PVA/mucin layer of our film could generate a stealth effect to avoid immune recognition and thus should help preventing acute inflammation reactions. Taken together, the different cytokine expression patterns we find on the opposing surfaces of the Janus-type film suggest that the bilayer construct can support wound repair processes by initiating a desirable immune response—but only where required.

Having analyzed different aspects of how both, eukaryotic and prokaryotic cells, interact with the two sides of the bilayer film, we now ask if the adhesive properties of the sticky layer might interfere with the ability of a damaged tissue layer to regenerate. To test this, we evaluate the ability of an artificially damaged cellular monolayer to “heal” itself when covered with a sticky bilayer film. As our results show, within 24 h, a combination of cell proliferation and migration effects efficiently close the gap in such a cellular monolayer (Figure 4e); the result only slightly depends on whether or not the cell layer is covered with a (drug-loaded or drug-free) bilayer film. Interestingly, film-treated groups show a slightly higher gap closure rate than the control group. Possibly, the hyaluronic acid molecules constituting the sticky layer matrix are responsible for this: HA has been found to be an important regulator of the re-epithelization process of tissues by affecting various intracellular pathways that control proliferation and migration.<sup>[62–64]</sup> Thus, both biomacromolecules constituting the film (HA and mucin) contribute to the properties of the construct by adding distinctive features to the respective surface of the bilayer material: while the fibrous PVA/mucin layer reduces protein adsorption, bacterial attachment, and uncontrolled cell adhesion, the d-HA side of the film promotes wound healing—at least in an in vitro model setting (Figure 4f).

Thus, in the next step, we investigate the wound healing performance of the Janus-type bilayer films in vivo by applying them to skin wounds that were created on the backs of rats. Here, we test full bilayer constructs to prevent unwanted adhesions to covering bandages that are applied around the created wounds (to prevent the rats from interfering with the wound healing process by scratching) while guaranteeing successful adhesion to the wound tissue. To allow for a better comparison of untreated and film-assisted wound healing processes, we generate two circular wounds (with a diameter of 1 cm each) on the dorsal side of each animal and cover one of those defects with a Janus-type film (either with an unloaded or antibiotic-loaded variant,  $N = 7$  wounds each) while leaving the other one uncovered (Figure 5a, left; see Figure S10 of the Supporting Information for an exemplary documentation of the

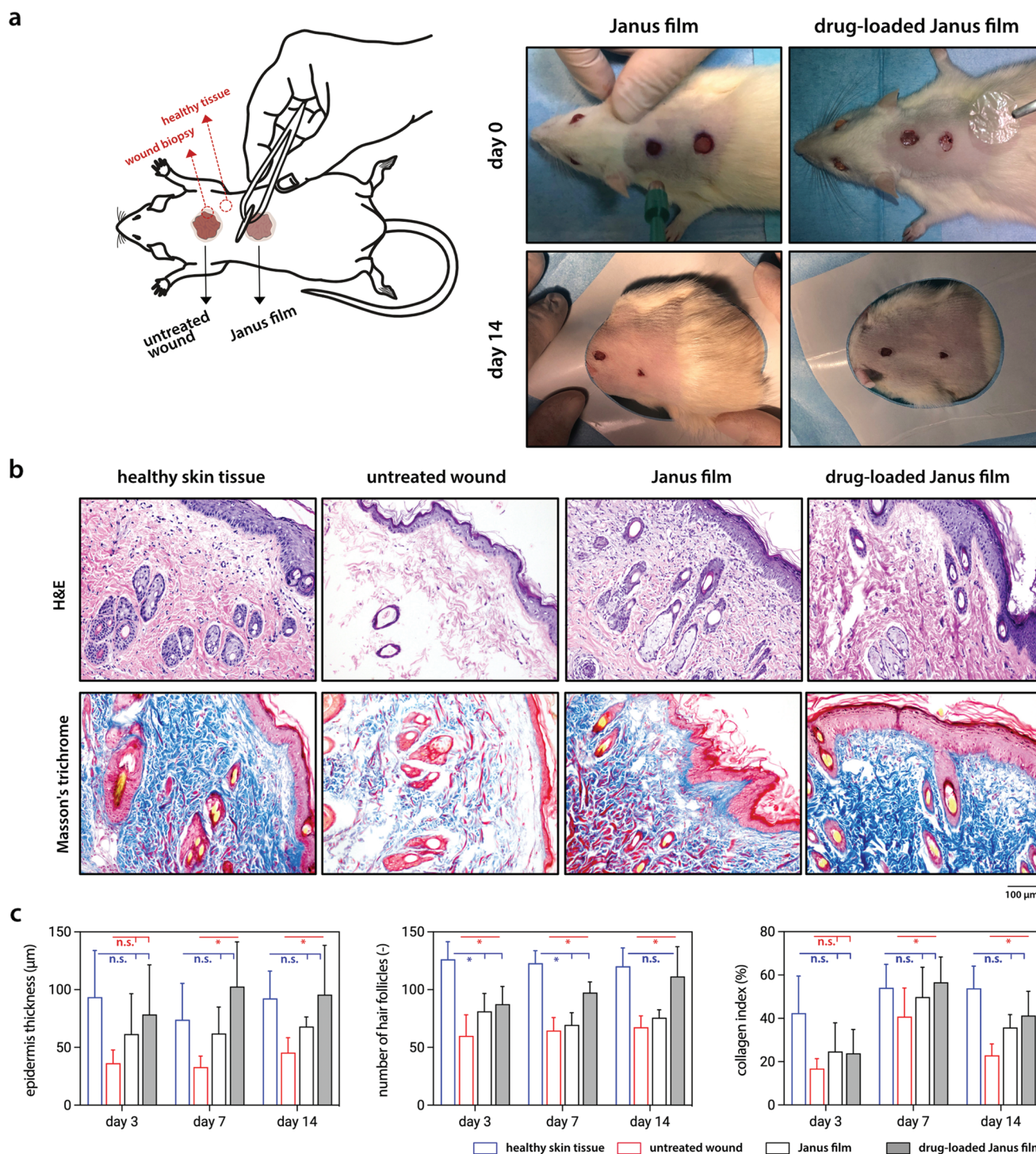


**Figure 5.** In vivo wound healing performance as observed by the application of Janus-type bilayer films to Sprague-Dawley rats. a) Schematic representation of untreated and film-treated wounds on the back of rats; representative images acquired on different postoperation (day 0 and 14) days images visualize the direct comparison of healing process of untreated wounds (left lesion) and film treated wounds (right lesion). b) Results of hematoxyline and eosin (H&E, top line) as well as Masson's trichrome stainings (bottom line) of different skin samples taken on the 14th day. The scale bar denotes 100  $\mu$ m and applies to all histology images. c) Quantitative assessments (epidermis thickness, number of hair follicles, and the collagen index) of H&E and Masson's trichrome stained tissue sections. Red lines indicate a statistical significance compared to the untreated wound; blue lines indicate a comparison with the healthy skin tissue. Data shown in the histograms represents mean values of parameters determined from  $N = 6$  animals per group (from each animal, ten histological images were analyzed); error bars denote the standard deviation. For each observation day, mean values obtained for Janus-type or drug-loaded Janus-type films were compared to values obtained for healthy skin tissue and untreated wound tissue by using Tukey's multiple comparisons test. Asterisks mark statistically significant differences based on a  $p$ -value of 0.05.



individual steps). As expected, when brought into contact with the wound tissue, the Janus-type bilayer films are able to adhere tightly without requiring additional fixation (see Video S3, Supporting Information). Our observations over a time span of 14 days reveal that Janus-type bilayer film treatment accelerates the healing process, which is in line with the results obtained from the *in vitro* tests: when wounds treated with films are compared to those of the untreated group, an improvement of the wound healing process is observed on the 14th postoperative day (Figure 5a, right). Compared to other materials tested for wet tissue adhesive applications,<sup>[16,65–67]</sup> the wound healing performance of the Janus-type bilayer films presented here is quite promising since the material itself promotes wound closure without the need of adding a stimulating agent such as growth factors.

To analyze the efficiency of the wound healing progress in more detail, biopsies are taken from the wounds at several stages of the healing process. Those tissue sections are stained with hematoxylin and eosin (H&E) and Masson's trichrome and then subjected to a histological evaluation (Figure 5b; Figure S11, Supporting Information); here, samples obtained from film-treated wounds are compared to both, untreated wound areas, and healthy skin tissue sections. For all groups, H&E staining indicates the presence of healthy corpuscles, hair follicles and blood vessels. Of course, as expected, the number of hair follicles in the wound zone is significantly smaller than in the healthy skin tissue. Notably, at day 14 of healing, wounds treated with films do not significantly differ anymore from healthy skin tissue in terms of epidermis thickness, number of hair follicles, and collagen index (Figure 5c). The observed wound healing performance is very similar for both, antibiotic loaded and antibiotic-free film variants. However, in a scenario where the tissue defect might already be challenged by a bacterial attack (i.e., under infection conditions), the application of an antibiotic-loaded Janus-type bilayer film should be beneficial to combat such existing wound infections, i.e., by canalizing the delivery of antibiotics to the wound site and by preventing bacterial adhesion on the opposing site.

These observations strongly underscore the excellent biocompatibility of the Janus-type bilayer films. In addition, at the 14th day after treatment, we observe successful hair regeneration in the healed area without any visible scar formation; we would like to emphasize that the applied Janus-type films were not removed manually—they degraded on their own thus making way for new tissue to grow (Figure S11, Supporting Information). Of course, depending on the application site, the degradation period of the films can vary. However, based on the findings shown here, it can be expected that the degradation products of the film do not impair tissue regrowth.

Having confirmed the ability of our films to promote wound healing *in vivo*, we next quantify the adhesive properties of the bilayer film when brought into contact with different tissues. In detail, we test porcine cornea, tongue, intestine, and cartilage samples, all of which exhibit a (geometrically) complex surface. Porcine tissue samples are selected due to their size and geometric similarity to human tissues. In those adhesion tests, we bring the bilayer film in contact with the selected tissue sample, allow the film to remain attached for a few seconds without applying any pulling force, and then retract the film at a

constant pulling rate. Although the mechanical sensitivity of adhesives is typically highest in this particular loading direction, we prefer this technique over the more commonly used lap shear tests: the lap shear tests are typically employed when two tissue samples are glued to each other (e.g., skin on skin, or muscle tissue on muscle tissue)<sup>[9,10,65,68]</sup>—and this requires the tissue samples to be properly fixated in the testing setup. Whereas easily possible for flat samples, this is trickier for tissues having complex geometries (such as eyeballs and tongues).

When we subject different variants/subcomponents of the bilayer film to the detachment test, we observe the following behavior: a d-HA monolayer has good adhesive properties; however, it ruptures during the detachment tests before any peeling sets in (Figure S5, Supporting Information). This behavior is not surprising since the d-HA layer forms an unstable gel when brought into contact with a wet tissue. Thus, it cannot withstand the stretching forces it is exposed to during the detachment test. Different from an adhesive that is supposed to connect two tissue samples, this would be problematic for the application envisioned here: the film would stick to fingers or tools during its application, which renders handling complicated. In contrast, the bilayer films are both, sticky and robust, i.e., they adhere well to tissues (even to those with complex topologies, see Figure 6a and Video S2, Supporting Information) but do not rupture as easily as simple d-HA films. Overall, we observe a good adhesion behavior. The adhesion energies we calculated from the detachment curves are highest for the tongue samples ( $\approx 4 \times 10^{-3}$  mJ mm<sup>-2</sup>), and a bit lower for intestine and eye samples ( $\approx 2.4 \times 10^{-3}$  and  $\approx 1.7 \times 10^{-3}$  mJ mm<sup>-2</sup>, respectively). Also, the detachment forces at which the bilayer films are removed from the tissues are very similar; this underscores the versatility of catechol-based adhesives as we use them here (Figure 6b). Additionally, control experiments performed with bilayer films containing a bottom layer of pristine, unmodified HA showed that catechol conjugation to HA is essential to obtain good adhesive behavior (Figure S4, Supporting Information).

Interestingly, the application of the bilayer film is not limited to tissues covered with wet epithelia: additional tests performed with cartilage samples show that the same bilayer construct can adhere to this particular tissue as well. For this group, we determine adhesion energy of  $\approx 1.3 \times 10^{-3}$  mJ mm<sup>-2</sup>. Indeed, an adhesive bilayer film could be applied to lateral areas of, e.g., knee joints, after osteochondral cylinders were transplanted into osteoarthritic areas of joints (i.e., when mosaicplasty with autografts is conducted). Moreover, it could be applied to other (nonarticular) cartilage surfaces located in, e.g., the face region. Here, such a bilayer film could protect implanted cartilage grafts from postoperation infections after reconstructive surgeries.

On a molecular scale, the strong and broad-range adhesion properties of the film are brought about by different interactions taking place between the catechol groups of dopamine and different chemical motifs present on the respective tissues. Those interactions include covalent, chemical bonds with  $-\text{NH}_2$  and  $-\text{SH}$  groups (as established by, e.g., Michael addition and Schiff base reactions<sup>[69]</sup>). In addition, dopamine can also engage in physical interactions with nucleophile groups (e.g., amines, thiol, imidazole) on the tissue surfaces.<sup>[70]</sup> Owing to the presence of the stabilizing PVA/mucin layer, the complete bilayer

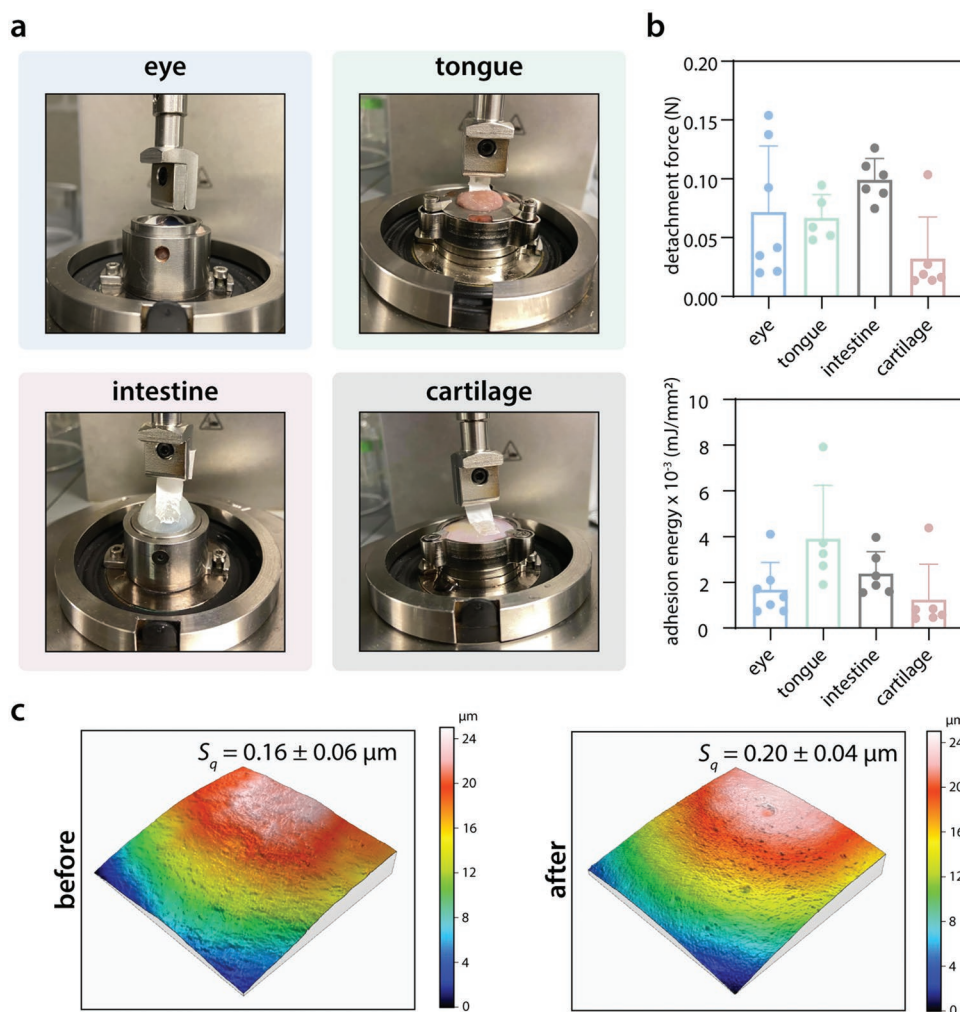


**Figure 6.** Detachment behavior of bilayer films from tissues. a) Ex vivo tissue detachment tests performed with porcine eye, tongue, intestine, and cartilage samples. The humidity chamber used for the measurements was removed for imaging. b) Detachment forces and adhesion energies as obtained for bilayer films (sticky side facing the tissue) when applied to and detached from different tissue samples. The data points denote individual measurements ( $n \geq 5$ ), vertical lines denote the standard deviation. c) Topographical 3D image of a representative cornea tissue sample before and after 3 days of treatment with a bilayer film (adhesive side facing the tissue). The numbers above the images denote average  $S_q$  values as determined from the images after the sample waviness was mathematically removed. Calculations are based on  $n = 5$  independent cornea samples, and error bars denote the standard deviation.

construct can be fully detached from the tissues without rupturing or leaving visible traces. When the detachment energy values from those peeling tests are calculated, we obtain comparable results for all tissues tested here, i.e., values in the range of 0.001–0.002 mJ mm<sup>-2</sup>. Those values agree well with previous results using a similar strategy to achieve tissue adhesion.<sup>[16]</sup> Moreover, adhesion energies with a similar order of magnitude were recently reported for bulk hydrogels employing polydopamine for adhesion promotion.<sup>[71]</sup> Other studies exploring bulk hydrogels as tissue adhesives were able to achieve even higher adhesion strengths,<sup>[72,73]</sup> but aimed at the long-term fixation of mechanically highly stressed tissues such as tendons<sup>[25]</sup> rather than short-term wound healing. Importantly, with the nonadhesive fibrous layer degrading slower than the adhesive d-HA layer (Figure 3a), it is reasonable to assume that this upper mucin-based layer prevents other tissues (e.g., the eyelid, when

the film is applied to the ocular cornea) from adhering to any film-treated tissue area while the bilayer film is present.

In practice, adhesive films are widely applied to tissues with quick healing abilities such as buccal mucosa or skin. Here, slight alterations in the surface structure of the tissue after wound healing are not a big issue, and any residues of the adhesive can easily be removed by the natural regeneration of the mucus layer or by manual rubbing. However, delicate tissues such as the ocular cornea are more sensitive, and any traces of material residues must be avoided. Even microscopic surface alterations would be detrimental for the optical function of the eye. Thus, in a final step, we analyze the microtopography of porcine cornea surfaces that were treated with a bilayer film for 3 days. This treatment time corresponds to the time span the bilayer film requires for efficient degradation in full immersion conditions. Probably, this degradation time can

be accelerated under dynamic conditions (e.g., when the film is exposed to continuous mechanical challenge such as blinking) that the film would encounter *in vivo*. However, in case a particular application calls for an extended lifetime, the supporting nonadhesive layer can be reinforced by incorporating other, more durable polymers into the mucin matrix, e.g., polycaprolactone instead of PVA.

To assess any alterations in the topography of the corneal tissue samples, we quantify 3D images obtained via light profilometry using established metrological parameters. This analysis shows that indeed, a bilayer film treatment (as well as its degradation products generated during film decomposition) does not induce a microtopographical change on the porcine cornea. This is demonstrated by very similar values calculated for the roughness parameter  $S_q$  (Figure 6c) and confirmed by a set of additional surface parameters that can define small pits and very fine scratches<sup>[74,75]</sup> (e.g., the surface area development, the isotropy of the surface, Table S2, Figure S6, Supporting Information). Together, these results show that—when autonomously degrading on the ocular cornea tissue—the bilayer film does not damage the tissue surface. The findings suggest that the material developed here is a very promising candidate for local drug delivery on sensitive body areas, where patient discomfort would severely limit the applicability of such a drug-loaded film.

### 3. Conclusion

In this work, we introduce a bilayer film that tackles core paradigms of wound management in a simple, yet, effective way. Owing to its asymmetric design, the bilayer film can fulfill distinct and indeed, contradictory physical and biological tasks even on complex and sensitive tissue surfaces.

With the macromolecular architecture and the bilayer design of the Janus-type films, it is not only possible to tailor the properties of the film to enable material adhesion; cellular migration, and drug release on the bottom side of the film, i.e., where wounded tissues would be treated, are possible. By contrast, the top layer of the film is here designed to achieve a stealth effect to minimize cellular immune response and to canalize the therapeutic and adhesive properties of the material to the desired area. Importantly, the mucin macromolecules present in this top layer would also allow for integrating a dynamic response into this top layer to meet additional, specific demands. For example, conformational changes of such mucin glycoproteins in combination with transiently stabilizing agents can be employed to encapsulate a wide variety of substances (hydrophilic, hydrophobic, charged, uncharged) into mucin films and to release them into surrounding tissues upon exposure to a trigger molecule.<sup>[76]</sup> The ability of these films to accelerate wound healing combined with their bacteria repellent surface properties makes them ideal candidates to prevent postoperative infections and to boost the tissue healing process. Additionally, as an alternative to a postinjury application, multifunctional Janus-type films could also be considered as interface materials mediating between wet tissues and artificial objects that are placed into the human body for extended time periods, e.g., wearable electronics such as glucose monitoring

devices. In conclusion, Janus-type bilayer films as we describe them here can be a promising alternative for patients or caregivers alike.

### 4. Experimental Section

**Dopamine–Hyaluronic Acid Conjugation:** A dopamine/hyaluronic acid conjugate (d-HA) was prepared as described previously with slight modifications.<sup>[77]</sup> In brief, hyaluronic acid sodium salt from *Streptococcus equi* (HA; Alfa Aesar, Ward Hill, MA, USA) was dissolved to a concentration of 1 % (w/v) in 2-(*N*-morpholino)ethanesulfonic acid (MES) buffer ( $10 \times 10^{-3}$  M, pH = 5). Afterward,  $5 \times 10^{-3}$  M 1-ethyl-3-(3-dimethylaminopropyl)carbo-diimide (EDC, Carl Roth, Karlsruhe, Germany) and  $5 \times 10^{-3}$  M *N*-hydroxysulfosuccinimide (sulfo-NHS, abcr, Karlsruhe, Germany) were added to this solution. After 3 h of incubation, this solution was mixed with 1% (w/v) dopamine hydrochloride (Sigma-Aldrich, St. Louis, MI, USA) solution (dissolved in  $5 \times$  PBS, pH = 8), at a volumetric ratio of 1:1, and then incubated during shaking at 4 °C overnight. On the next day, the solution was transferred into dialysis tubes (MWCO = 300 kDa, Thermo Fisher Scientific, Waltham, MA, USA) and dialyzed against ultrapure water at 4 °C for two days. The dialyzed samples were freeze-dried for 2 days and stored at  $-80$  °C until further use. The degree of catechol functionalization achieved with this procedure was determined spectrophotometrically by converting the absorbance value of d-HA solutions at 280 nm to a concentration value using a linear calibration curve obtained for pure dopamine solutions of different concentrations. Those absorption measurements were conducted on a specord 210 spectral photometer (Analytikjena, Jena, Germany).

**Production of Bilayer Films:** To generate the adhesive layer of the bilayer film, d-HA was solubilized in ddH<sub>2</sub>O ( $10 \text{ mg mL}^{-1}$ ) and poured into a custom-made polycarbonate 6-well plate. Then, the solution in the wells was degassed under vacuum and left to dry at air at room temperature (RT) for 2 days. In the next step, the fibrous layer was generated by electrospinning a PVA/mucin solution onto a preformed d-HA film. To do so, first, PVA (500 mg, MW:  $\approx 145\,000 \text{ g mol}^{-1}$ , Sigma-Aldrich) was solubilized in ddH<sub>2</sub>O (5 mL) at 80 °C for 1 h; then, the solution was allowed to cool down to RT. Next, manually purified mucin (25 mg, MUC5AC, see the Supporting Information for MUC5AC purification) was solubilized in ddH<sub>2</sub>O (5 mL) and gradually added to the PVA solution. Per sample,  $\approx 0.25$  mL of the final solution was deposited onto the preformed d-HA layer using a custom-made, laboratory-scale, vertical electrospinning device. The parameters of this process were selected as follows: voltage, 15 kV; distance between collector and syringe, 10 cm; flow rate,  $0.03 \text{ mL min}^{-1}$ . The final bilayer structure was stabilized by cross-linking the macromolecular components through exposure to glutaraldehyde (GA; 25 % aqueous solution, Sigma-Aldrich) vapor at RT for 12 h, followed by an incubation step in a vacuum chamber for 4 h. Completed samples were stored in a desiccator until further use.

**Bilayer Film Characterization: Morphology:** The morphology of the fibrous mat and the bilayer film was characterized using scanning electron microscopy (SEM; JEOL-JSM-6060LV, Jeol, Echting, Germany). Prior to tests, samples were coated with a thin gold layer using an MED 020 sputtering device (BAL-TEC, Balzers, Liechtenstein) under a saturated argon gas atmosphere. The diameter of PVA/MUC nanofibers was determined from those SEM images using the software ImageJ. Confocal laser scanning microscopy was used to quantitatively assess the isotropy of the fibrous layer (see the Supporting Information).

**Wetting Properties:** The wetting behavior of the samples was tested by contact angle measurements using a drop shape analyzer device (DSA25S, Krüss GmbH, Hamburg, Germany). For examination, samples were placed in front of the device-integrated high-resolution camera (acA1920, Basler, Ahrensburg, Germany). Imaging, processing, and image analysis were performed with the software ADVANCE (AD4021 v1.13, Krüss GmbH), which was used to initiate automatic imaging (15 fps for 5 s) once a droplet ( $4 \mu\text{L ddH}_2\text{O}$ ) crossed a trigger line positioned just above the sample surface. 0.5 s after the first image of a

droplet (uninfluenced by the cannula) was captured, the images captured within the next 1.5 s were analyzed using the software-integrated ellipse (tangent-1) fit method. Contact angle values were determined as the water-enclosed angle between the surface and the edge of the droplet.

**Mechanical Characterization:** The tensile properties of the films (both, bilayer, and individual monolayers) were tested under uniaxial tension using a research-grade shear rheometer (MCR 302, Anton Paar, Graz Austria). In brief, rectangular samples were prepared by casting the adhesive layers in rectangular (10 mm × 30 mm) molds fabricated from polycarbonate. The measurements were performed by fixing the films at either end in custom-made clamp-like sample holders. The first of those clamps were fixed to the central shaft of the rheometer using a commercial adapter (D-CP/PP 7, Anton Paar); the second clamp was mounted onto a commercial bottom plate (P-PTD 200, Anton Paar). The measurement head of the rheometer was lifted at a constant speed of 10 μm s<sup>-1</sup> until the film was ruptured, and the resulting normal force data were recorded at a sampling rate of 1/s (see Figure S6, Supporting Information, for the setup).

To evaluate the mechanical robustness of the films under tribological stress, they were probed in an oscillatory tribology setup as described in Winkeljann et al.<sup>[78]</sup> and subsequently examined optically. Here, both counterparts of the setup, i.e., polydimethylsiloxane (PDMS, SYLGARD 184, Dow Corning) pins with rounded edges in the measuring head and kidney-shaped PDMS samples in the sample holder, were cast in custom-made molds, activated by exposure to atmospheric plasma in a SmartPlasma2 oven (plasma technology GmbH, Herrenberg, Germany; settings: 0.4 mbar, 30 W, 1.5 min) to become hydrophilic,<sup>[79]</sup> and stored in ddH<sub>2</sub>O until further use to avoid hydrophobic recovery.<sup>[79,80]</sup> d-HA and bilayer films were cast in circular molds (Ø = 20 mm) made from polycarbonate, and circular samples (Ø = 10 mm) were punched from the central areas of these films with a hand press (IstaBreeze Germany GmbH, Bad Rappenau, Germany). Before starting a measurement, the film samples were first hydrated in situ by applying each onto a moistened kidney-shaped PDMS sample. Then, 40 μL of PBS was added as a lubricant, and the friction response of the material pairing was recorded every 0.15 s in oscillatory mode over a deflection angle of 17° while applying a normal load *F* of 0.6 N, a sliding velocity of 0.7 mm s<sup>-1</sup>, and a temperature of 37 °C. With those parameters, the resulting contact pressure is ≈0.028 MPa. To avoid evaporation of the lubricant as well as film drying, a moisture trap was installed. As control samples, plasma-activated PDMS specimens were probed without any film added (using PBS as a lubricant).

Once the oscillatory tribology measurements were concluded, any excess liquid was gently removed from the films, and they were allowed to dry at RT for two days. For both, macroscopic and microscopic examination of the film surfaces, a confocal laser scanning microscope (VK-X1000, Keyence, Oberhausen, Germany) was used. Combined laser confocal/light microscopy images were captured at 20× magnification (CF Plan, NA = 0.46; Nikon, Chiyoda, Tokyo, Japan). For obtaining a macroscopic overview of the films, several images acquired at 5× magnification (CF Plan, NA = 0.13; Nikon) were stitched together. The projected area of the films was determined using the open-source software ImageJ.

**Degradation Behavior:** For each layer of the bilayer film, the degradation behavior was assessed spectrophotometrically. To distinguish between the degradation products originating from either layer, chemical groups specific for each layer were selected, and their particular absorbance spectrum was tracked as they enter the liquid phase in which the bilayer samples were incubated. To represent the nonadhesive layer, a fluorescent dye covalently attached to mucins (Atto 488 – carboxy modified, ATTO-TEC GmbH, Siegen, Germany; Ex/Em = 488/535 nm) via carbodiimide coupling was selected (see the Supporting Information). To represent the adhesive layer, catechol groups (absorbance at 280 nm) were tracked. Samples immersed into aqueous solutions (see above) were placed onto an orbital shaker operating at 37 °C while avoiding light exposure. The supernatants were collected at predetermined time intervals and characterized using a multilabel plate reader (Victor3, Perkin Elmer, Rodgau, Germany). To evaluate the degradation profile of the d-HA layer, PVA/mucin monolayers were incubated under similar

conditions and their absorbance (at 280 nm) was subtracted from those obtained with d-HA films to avoid any interference.

**Swelling Profile:** For swelling tests, the measuring setup of the drop shape analyzer device used for the evaluation of the wetting behavior of the films was employed; also here, transversal images of the cross-section of the bilayer film were obtained and evaluated during the swelling process of the material. In detail, bilayer films were punched into circular samples (Ø 7 mm) using a manual eyelet press (IstaBreeze Germany GmbH, Bad Rappenau, Germany); then, the initial height of each sample was measured using a digital caliper, and the initial cross-section of each sample was determined in a dry state. Afterward, a piece of lint-free laboratory wipe (≈6 cm × 6 cm) was fixated on a glass slide using adhesive tape to impede wrinkling of the laboratory wipe, and 750 μL of ddH<sub>2</sub>O was added to fully wet the laboratory wipe. Then, the bilayer film samples (with the mucin/PVA side facing downward to prevent the films from rolling up during hydration) were placed onto the laboratory wipe, and images were automatically captured at different time steps for a total duration of 30 min. For evaluating the swelling behavior of each sample, *t* = 0 s was defined by the first image of the bilayer construct being in contact with the wet wipe. The captured images (including a scale bar) were exported using the ADVANCE software and were analyzed with the software ImageJ (version 1.53k) by setting the scale according to the displayed scale bar; here, the contrast was increased to 0.3% saturated pixels by enabling the option “equalize histogram.” Then, the cross-sectional area was determined by identifying the outlines of the sample manually. Prior to averaging the results obtained from different film samples, the cross-sections measured at each time-step were normalized to the initial cross-section determined for each sample in a dry state.

**Drug Loading and In Vitro Drug Release:** TCL (Applichem, Darmstadt, Germany) was chosen as a model antibiotic and solubilized in a d-HA solution (0.86 mg mL<sup>-1</sup>) before casting the bottom layer of the bilayer film. With this concentration of TCL in the d-HA solution, the expected TCL concentration in the bilayer film is ≈5.5 μg mm<sup>-2</sup>. After the formation of the bilayer films, they were placed into wells of a 24-well plate equipped with permeable insert strips (BRANDplates insert system, pore size: 0.4 μm, Brand, Wertheim, Germany) to test their in vitro drug release behavior. The in vitro TCL release profile was determined by placing the TCL-loaded bilayer films into a range of solutions: simulated tear fluid, STF (NaCl: 6.78 g L<sup>-1</sup>, NaHCO<sub>3</sub>: 2.18 g L<sup>-1</sup>, CaCl<sub>2</sub>·2H<sub>2</sub>O: 0.084 g L<sup>-1</sup>, KCl: 1.38 g L<sup>-1</sup>, pH = 7.4); saliva mimetic, HSM (0.02% (w/v) manually purified human salivary MUC5B dissolved in 20 × 10<sup>-3</sup> M TRIS, pH = 7.4; see the Supporting Information for MUC5B purification); SIF (KH<sub>2</sub>PO<sub>4</sub>: 6.8 g L<sup>-1</sup>, NaOH: 0.896 g L<sup>-1</sup>, pH = 6.8), and phosphate buffer saline, PBS (pH = 7.4). To mimic the salivary conditions with HSM, human salivary mucin (0.02% w/v in 20 × 10<sup>-3</sup> M TRIS, pH = 7.4) was used manually purified to mimic the typical pH range and the average mucin concentration of human saliva.<sup>[81]</sup> Together, this set of solutions mimics the range of environmental conditions the bilayer film may encounter in an in vivo setting. The drug release quantification was then conducted as follows: the bilayer films were hydrated with 200 μL of the respective aqueous solution first; then, 2 mL of the same solution medium was placed into the bottom part of the chamber so that the bottom (drug-loaded) part of the bilayer film is fully wetted from below and can release drugs into this bottom part of the chamber over time. The absorbance of the liquid in this bottom chamber was then quantified at 360 nm at predetermined time intervals with a spectrophotometer (specord 210, Analytikjena, Jena, Germany) to detect drug molecules entering this liquid phase via diffusion. The released drug amount was quantified by converting the absorbance values of this liquid phase into absolute concentration values based on a TCL standard curve (Figure S8, Supporting Information).

**Protein Adsorption:** To assess the protein adsorption behavior to either side of the bilayer construct, a model protein, i.e., BSA (Albumin fraction V, Carl Roth) labeled with Atto488 (see the Supporting Information) was selected. The d-HA and PVA/mucin layers of the bilayer film were created separately, and each component was studied independently. Monolayer samples were placed into wells of a 24-well plate and incubated with

a fluorescently labeled BSA solution (0.1% (w/v) in PBS). Then, the samples were placed onto an orbital shaker while avoiding light and incubated at 37 °C for 1 h. After incubation, the supernatants were collected, and the fluorescence signal of this supernatant was quantified using a multilabel plate reader at Ex/Em = 488/535 nm. Then, the amount of BSA adsorbed onto the film was determined as the amount of fluorescent BSA depleted from the solution.

**In Vitro Experiments with Prokaryotic and Eucaryotic Cells:** Prior to all in vitro tests involving cells, the bilayer film samples were placed into a sterilization chamber (BLX-254, Vilber Lourmat GmbH, Eberhardzell, Germany) and exposed to UV light (254 nm, 5 × 8 W) for 3 h. If not stated otherwise, all chemicals used for those in vitro tests were purchased from Sigma-Aldrich. Those experiments were conducted with human epithelial (HeLa) cells cultured in minimum essential medium supplemented with 10% (v/v) fetal bovine serum, 2 × 10<sup>-3</sup> M L-glutamine solution, and 1% (v/v) nonessential amino acids. The cultivation of HeLa cells was conducted at 37 °C in a humidified atmosphere containing 5% CO<sub>2</sub>.

**Biocompatibility:** A live/dead assay was applied to assess the biocompatibility of each side of the bilayer films. Here, bilayer film samples were placed into wells of an 8-well plate (μ-Slide ibidiTreat plate, ibidi GmbH, Gräfelfing, Germany), HeLa cells were seeded onto either the adhesive or the nonadhesive side of the bilayer film (30000 cells per sample) and incubated for 24 h. Next, the samples were washed with DPBS and stained with 100 μL per well of a live/dead solution (1 × 10<sup>-6</sup> M calcein-AM, 2 × 10<sup>-6</sup> M ethidium homodimer 1, Invitrogen, Carlsbad, CA, USA). After 30 min of incubation, fluorescence images were acquired on a fluorescence microscope (DMI8, Leica, Wetzlar, Germany) using FITC (Ex = 460–500, DC = 505; Em = 512–542, Leica) and TXR filter cubes (Ex = 540–580, DC = 585; Em = 592 – 668, Leica), respectively. The exposure times were first optimized for each filter set and applied to all acquired images.

**Bacterial Adhesion:** Bacterial attachment tests were conducted with the strains *S. aureus* NCTC 8325-4 and *E. coli* ATCC 25922. Frozen vials containing bacteria at concentrations of 10<sup>8</sup> CFU mL<sup>-1</sup> were reconstituted in PBS. The bilayer film samples were sterilized under UV light at a wavelength of 254 nm for 2 h. The bacterial suspensions were subsequently inoculated at a concentration of 10<sup>7</sup> CFU mL<sup>-1</sup> onto the layer to be tested, i.e., the fibrous PVA/MUC layer and the d-HA layer, respectively. The samples were incubated at 37 °C for 2 h. Nonadherent bacteria were removed by washing the samples thrice in 5 mL sterile PBS. Then, the samples were vortexed in PBS for 1 min to remove the adherent bacteria, and the obtained suspensions were serially diluted. These serial dilutions were plated onto tryptic soy agar plates, which were incubated at 37 °C for 24 h. After this incubation period, the colonies were counted to determine the number of adherent bacteria for either sample layer.

**In Vitro Cell Scratch Assay:** An in vitro scratch test using cellular monolayers was applied to ensure that the sticky properties of the bilayer film do not prevent wound healing. First, HeLa cells were cultivated in a 48-well plate (80000 cells per well) for 24 h. Then, a horizontal scratch was created in the middle part of the well using a pipette tip and a bilayer film was placed on top of this scratched cell layer (with the sticky side facing the cellular layer). The time-dependent closure of the damaged cell layer was observed on an inverted light microscope (DMI8, Leica) equipped with a 10× objective (Leica) and a digital camera (Orca Flash 4.0 C11440, Hamamatsu, Japan); images were acquired after 6, 12, and 24 h of incubation. As a control, scratched cellular layers without an additional bilayer film were used.

**Pro/Anti-Inflammatory Cytokine Release of Macrophages In Vitro:** The immune response to the bilayer system was evaluated by determining the cytokine expression of monocyte-derived macrophages. The human cell line U937 (ATCC) was cultured in RPMI 1640 medium (Gibco, Life Technologies, Paisley, UK) supplemented with 10% fetal calf serum (Gibco), 2 × 10<sup>-3</sup> M L-glutamine (Gibco), 1 × 10<sup>-3</sup> M sodium pyruvate (Gibco), 1 U mL<sup>-1</sup> penicillin and 1 μg mL<sup>-1</sup> streptomycin (Gibco). The cells were then differentiated into M0 macrophages using 100 × 10<sup>-9</sup> M phorbol 12-myristate 13-acetate for 72 h and were allowed to rest in

a complete culture medium for 24 h before the assay was conducted. These monocyte-derived M0 macrophages were seeded at a density of 800000 cells mL<sup>-1</sup> onto the samples, and the cytokine concentration in the macrophage culture supernatant was evaluated after 24 and 72 h of incubation at 37 °C with 5% CO<sub>2</sub>. Quantification of the released proinflammatory (interleukin-6, tumor necrosis factor-α) and anti-inflammatory (interleukin-1 receptor antagonist, interleukin-10) cytokines was performed with the DuoSetELISA Development System (R&D Systems, Minneapolis, MN, USA) following the manufacturer's instructions using a multimode microplate reader (Spark, Tecan, Männedorf, Switzerland).

**In Vivo Wound Healing Experiments:** Prior to in vivo experiments, all film samples were sterilized by ethylene oxide exposure. The experimental protocol of the study was reviewed and approved by the Animal Experiments Local Ethics Committee of Bagcilar Training and Research Hospital (decision number: 2021/116). All procedures were applied according to the guide for the care and use of laboratory animals adopted by the National Institutes of Health (USA) and the Declaration of Helsinki. Tests were performed with Sprague-Dawley rats (body weight, 250–350 g, N = 14) at the University of Health Sciences, Bagcilar Training and Research Hospital Research Center, Istanbul, Turkey. The animals were housed in a controlled environment at a temperature of (24 ± 2) °C and at a humidity of 60% under a 12 h light/dark cycle. The animals were given free access to water and standard nutrition. The rats were anesthetized by intraperitoneal administration of ketamine/xylazine (90/10 mg kg<sup>-1</sup>), and all efforts were made to minimize animal suffering. Prior to the experiments, the backs of the rats were shaved; then, two full-thickness skin defects (including epidermis and dermis) were created on the dorsal side of each rat using a 12 mm biopsy punch. One of the such created wounds was covered with a Janus-type bilayer film (either plain or antibiotic loaded, N = 7 each), and the defects were covered with a bandage to avoid uncontrolled animal reactions such as scratching or biting. On the 3rd, 7th, and 14th day of wound regeneration, a tissue sample was taken from both, the wound areas and a healthy skin tissue area using a 3 mm biopsy punch; those samples were fixed with paraformaldehyde (4% v/v) and then subjected to further histopathological examinations. To do so, 5 μm thick sections from paraffin-embedded tissue samples were stained with Harris hematoxylin/eosin and Masson trichrome (both obtained from Bio-Optika S.p.A, Milan, Italy) using routine procedures and afterward examined under a light microscope (Olympus BX53, Melville, NY, USA). The maximal epidermis thickness per image, the total number of hair follicles, and the average collagen density per image were calculated using the software ImageJ by analyzing n = 10 images per animal (N = 6) at each day of observation (day 0, 3, 7, and 14). Findings obtained with film treated samples were compared to untreated wounds and healthy skin tissue using a paired t-test; significant differences were marked with an asterisk if based on a p-value of p ≤ 0.05.

**Experiments Involving Ex Vivo Tissue Samples: Tissue Adhesion/Detachment Tests:** Adhesion/detachment tests were performed on a commercial research-grade shear rheometer (MCR 302, Anton Paar, Graz Austria). Different ex vivo tissue samples (porcine eye, tongue, intestine, and cartilage samples) were tested, which were all obtained from a local butcher shop. The tissue samples were placed into a custom-made sample holder mounted to a commercial bottom plate (T-PTD 200, Anton Paar). In this step, the surface of each sample was smoothed by fixing the tissue with a stainless-steel ring; this step was necessary to remove macroscopic wrinkles on the tissue surface, which otherwise could negatively affect the adhesion/detachment test by rendering it less reproducible. Before mounting the samples into the sample holder, they were first hydrated with PBS. Then, the adhesion/detachment tests were conducted in a humidified atmosphere at a constant temperature of 37 °C. The bilayer film sample was fixed to the measuring shaft of the rheometer by attaching a custom-made clamp (see the Supporting Information) fabricated in a local workshop to a commercial adapter (D-CP/PP 7, Anton Paar). For each measurement, a fresh bilayer film and a fresh tissue sample were used. Each detachment test was then conducted as follows: the measuring head of the rheometer was lowered

until one side of the bilayer film (either its adhesive or nonadhesive side) was brought into contact with the tissue (the contact area was  $\approx 64 \text{ mm}^2$ ). This contact was maintained for 10 s; afterward, the measuring head was lifted at a constant speed of  $10 \mu\text{m s}^{-1}$ , and the resulting normal force was recorded at a measuring point density of 1/s until the measured force dropped to zero. The adhesion energy was calculated from the force–distance plot by calculating the area under the force–distance curve.

**Topographical Evaluation of Bilayer Film-Treated Cornea Tissues:** To assess whether the bilayer film would leave any residues or surface damage on a tissue after the film has been degraded, a topographical evaluation was performed. Here, porcine cornea samples were selected as they represent a particularly sensitive tissue variant. In detail, each sample was evaluated twice, i.e., before and after having been in contact with the adhesive side of a bilayer film for 3 days. To do so, fresh porcine eyes were first incubated in an antibiotic solution (0.2% TCL) for 1 h, gently rinsed with PBS, and kept on a tissue cloth for  $\approx 10 \text{ min}$  (to allow water droplets on the surface to evaporate). After eliminating the eye samples which exhibited visible, macroscopic defects, profilometric images of the corneal surfaces were obtained using a laser scanning microscope equipped with a 20 $\times$  lens. For each sample, five images were acquired. Image quantification was then performed using the  $\mu$ soft analysis extended software (version 7.2.7568, NanoFokus AG, Oberhausen, Germany). Prior to data analysis, a Gaussian filter (according to ISO 16610–61) with a cutoff wavelength of  $80 \mu\text{m}$  was applied. For each topographical image, the following metrological parameters were calculated: the root-mean-square height ( $S_q$ ), the developed interfacial area ratio ( $S_{dr}$ ), the isotropy of the surface ( $S_{tr}$ ), the maximum peak height ( $S_p$ ), the root mean square gradient ( $S_{dq}$ ), the arithmetic mean peak curvature ( $S_{pc}$ ), the peak material volume ( $V_{mp}$ ), and the dale void volume ( $V_{wv}$ ); those parameters are all defined in ISO 25178-2 (see the Supporting Information). From those assessments, the set of eye samples was further narrowed down by eliminating those which showed noticeable microscopic defects; in detail, those samples that returned a surface roughness parameter ( $S_q$ ) smaller than  $0.3 \mu\text{m}$  were selected. With this procedure, it could be ensured that the population of cornea samples studied here had comparable, well-defined initial properties. Then, bilayer films were placed onto the hydrated surfaces of the cornea samples, and the eyes were immersed in STF (supplemented with 0.2% TCL) at  $4 \text{ }^\circ\text{C}$  for 3 days until the bilayer films were fully degraded. As a control, similar incubation conditions were applied to a control group, i.e., eye samples that did not receive a film treatment. After 3 days of incubation, profilometric images were acquired again, and the same metrological parameters described above were calculated to quantify the effect of bilayer film treatment.

**Statistical Analysis:** The software GraphPad Prism (Prism 8, San Diego, CA, USA) was used to conduct all statistical analyses. All the data collected in this work were presented as mean  $\pm$  standard deviation. Before each analysis, the normal distribution of the measured values was confirmed with a Shapiro-Wilk test. A two-tailed Student's *t*-test was performed for normally distributed populations with homogeneous variances, whereas a two-tailed Welch's *t*-test was used in case of unequal variances. Tukey's multiple comparison test were conducted for the comparison between multiple samples. If not stated otherwise, a *p*-value of  $p \leq 0.05$  was chosen as a threshold for significance; accordingly, significant differences were marked with an asterisk where applicable.

## Supporting Information

Supporting Information is available from the Wiley Online Library or from the author.

## Acknowledgements

The authors thank Benjamin Winkeljann for designing custom-made sample molds, and Corinna Lieleg for helpful discussions regarding

histology assessments. This project was funded by the Deutsche Forschungsgemeinschaft (DFG, German Research Foundation)—SFB-863—Project ID 111166240 and Munich Multiscale Biofabrication Network.

Open access funding enabled and organized by Projekt DEAL.

## Conflict of Interest

The authors declare no conflict of interest.

## Author Contributions

The study was designed by C.K. and O.L. S.M. and P.M. designed the cytokine release experiments. M.G.B. conducted the tribology and swelling experiments. C.K. and M.B. performed the shearing tests and drug release studies. T.M.L. and S.M. performed experiments involving eukaryotic and prokaryotic cells. E.A., Z.D., and P.K. conducted the in vivo study. C.K. performed all other experiments and analyzed the data. The manuscript was written by C.K. and O.L. and was critically revised by all authors.

## Data Availability Statement

The data that support the findings of this study are available from the corresponding author upon reasonable request.

## Keywords

asymmetric designs, bioadhesives, hyaluronic acid, mucin, wound management

Received: June 14, 2021  
Revised: March 22, 2022  
Published online: April 30, 2022

- [1] A. R. Parker, C. R. Lawrence, *Nature* **2001**, 414, 33.
- [2] H.-C. Yang, Y. Xie, J. Hou, A. K. Cheetham, V. Chen, S. B. Darling, *Adv. Mater.* **2018**, 30, 1801495.
- [3] A.-Y. Lu, H. Zhu, J. Xiao, C.-P. Chuu, Y. Han, M.-H. Chiu, C.-C. Cheng, C.-W. Yang, K.-H. Wei, Y. Yang, Y. Wang, D. Sokaras, D. Nordlund, P. Yang, D. A. Muller, M.-Y. Chou, X. Zhang, L.-J. Li, *Nat. Nanotechnol.* **2017**, 12, 744.
- [4] A. Kirillova, C. Marschelke, A. Synytska, *ACS Appl. Mater. Interfaces* **2019**, 11, 9643.
- [5] W. Wu, R. Cheng, J. Das Neves, J. Tang, J. Xiao, Q. Ni, X. Liu, G. Pan, D. Li, W. Cui, B. Sarmiento, *J. Controlled Release* **2017**, 261, 318.
- [6] B. D. Ratner, *Annu. Rev. Biomed. Eng.* **2019**, 21, 171.
- [7] L. Wang, X. Zhang, K. Yang, Y. V. Fu, T. Xu, S. Li, D. Zhang, L. U.-N. Wang, C.-S. Lee, *Adv. Funct. Mater.* **2020**, 30, 1904156.
- [8] S. Li, N. Chen, X. Li, Y. Li, Z. Xie, Z. Ma, J. Zhao, X. Hou, X. Yuan, *Adv. Funct. Mater.* **2020**, 30, 2000130.
- [9] K. Xu, Y. Liu, S. Bu, T. Wu, Q. Chang, G. Singh, X. Cao, C. Deng, B. Li, G. Luo, M. Xing, *Adv. Healthcare Mater.* **2017**, 6, 1700132.
- [10] Y. Zhou, L. Gao, J. Peng, M. Xing, Y. Han, X. Wang, Y. Xu, J. Chang, *Adv. Healthcare Mater.* **2018**, 7, 1800144.
- [11] C. Gong, C. Lu, B. Li, M. Shan, G. Wu, *J. Biomed. Mater. Res., Part A* **2017**, 105, 1000.
- [12] T. M. Lutz, C. Kimna, A. Casini, O. Lieleg, *Mater. Today Bio* **2022**, 13, 100203.

- [13] X. Peng, X. Xia, X. Xu, X. Yang, B. Yang, P. Zhao, W. Yuan, P. W. Y. Chiu, L. Bian, *Sci. Adv.* **2021**, 7, 8739.
- [14] S. Hu, X. Pei, L. Duan, Z. Zhu, Y. Liu, J. Chen, T. Chen, P. Ji, Q. Wan, J. Wang, *Nat. Commun.* **2021**, 12, 1689.
- [15] W.-C. Huang, R. Ying, W. Wang, Y. Guo, Y. He, X. Mo, C. Xue, X. Mao, *Adv. Funct. Mater.* **2020**, 30, 2000644.
- [16] J. Shin, S. Choi, J. H. Kim, J. H. Cho, Y. Jin, S. Kim, S. Min, S. K. Kim, D. Choi, S.-W. Cho, *Adv. Funct. Mater.* **2019**, 29, 1903863.
- [17] M. M. Hasani-Sadrabadi, P. Sarrion, S. Pouraghaei, Y. Chau, S. Ansari, S. Li, T. Aghaloo, A. Moshaverinia, *Sci. Transl. Med.* **2020**, 12.
- [18] X. Zhao, Y. Liang, Y. Huang, J. He, Y. Han, B. Guo, *Adv. Funct. Mater.* **2020**, 30, 1910748.
- [19] T. Chen, Y. Chen, H. U. Rehman, Z. Chen, Z. Yang, M. Wang, H. Li, H. Liu, *ACS Appl. Mater. Interfaces* **2018**, 10, 33523.
- [20] C. Xuan, L. Hao, X. Liu, Y. Zhu, H. Yang, Y. Ren, L. Wang, T. Fujie, H. Wu, Y. Chen, X. Shi, C. Mao, *Biomaterials* **2020**, 252, 120018.
- [21] M. Li, Z. Zhang, Y. Liang, J. He, B. Guo, *ACS Appl. Mater. Interfaces* **2020**, 12, 35856.
- [22] C. Cui, T. Wu, X. Chen, Y. Liu, Y. Li, Z. Xu, C. Fan, W. Liu, *Adv. Funct. Mater.* **2020**, 30, 2005689.
- [23] B. Xu, A. Li, R. Wang, J. Zhang, Y. Ding, D. Pan, Z. Shen, *Adv. Funct. Mater.* **2021**, 31, 2105265.
- [24] G. U. Ruiz-Esparza, X. Wang, X. Zhang, S. Jimenez-Vazquez, L. Diaz-Gomez, A.-M. Lavoie, S. Afewerki, A. A. Fuentes-Baldemar, R. Parra-Saldivar, N. Jiang, N. Annabi, B. Saleh, A. K. Yetisen, A. Sheikhi, T. H. Jozefiak, S. R. Shin, N. Dong, A. Khademhosseini, *Nano-Micro Lett.* **2021**, 13, 1.
- [25] B. R. Freedman, A. Kuttler, N. Beckmann, S. Nam, D. Kent, M. Schulte, F. Ramazani, N. Accart, A. Rock, J. Li, M. Kurz, A. Fisch, T. Ullrich, M. W. Hast, Y. Tinguely, E. Weber, D. J. Mooney, *Nat. Biomed. Eng.* **2022**, 1.
- [26] W. Liang, W. He, R. Huang, Y. Tang, S. Li, B. Zheng, Y. Lin, Y. Lu, H. Wang, D. Wu, *Adv. Mater.* **2022**, 34, 2108992.
- [27] G. Petrou, T. Crouzier, *Biomater. Sci.* **2018**, 6, 2282.
- [28] J. A. Burdick, G. D. Prestwich, *Adv. Mater.* **2011**, 23, H41.
- [29] L. u Han, X. Lu, K. Liu, K. Wang, L. Fang, L. u-T. Weng, H. Zhang, Y. Tang, F. Ren, C. Zhao, G. Sun, R. Liang, Z. Li, *ACS Nano* **2017**, 11, 2561.
- [30] H. Lee, S. M. Dellatore, W. M. Miller, P. B. Messersmith, *Science* **2007**, 318, 426.
- [31] B. Winkeljann, M. G. Bauer, M. Marczyński, T. Rauh, S. A. Sieber, O. Lieleg, *Adv. Mater. Interfaces* **2020**, 7, 1902069.
- [32] R. Nudelman, H. Alhmoud, B. Delalat, S. Fleicher, E. Fine, T. Guliakhmedova, R. Elnathan, A. Nyska, N. H. Voelcker, M. Gozin, S. Richter, *Adv. Funct. Mater.* **2019**, 29, 1902783.
- [33] A. W. Nugroho, H. Sosiati, P. Wijongko, *Int. J.* **2011**, 8, 2431.
- [34] M. Marczyński, K. Jiang, M. Blakeley, V. Srivastava, F. Vilaplana, T. Crouzier, O. Lieleg, *Biomacromolecules* **2021**, 22, 1600.
- [35] L. Shi, R. Ardehali, K. D. Caldwell, P. Valint, *Colloids Surf., B* **2000**, 17, 229.
- [36] J. Y. Co, T. Crouzier, K. Ribbeck, *Adv. Mater. Interfaces* **2015**, 2, 1500179.
- [37] H. Yan, C. Seignez, M. Hjorth, B. Winkeljann, M. Blakeley, O. Lieleg, M. Phillipson, T. Crouzier, *Adv. Funct. Mater.* **2019**, 29, 1902581.
- [38] T. Crouzier, K. Boettcher, A. R. Geonnotti, N. L. Kavanaugh, J. B. Hirsch, K. Ribbeck, O. Lieleg, *Adv. Mater. Interfaces* **2015**, 2, 1500308.
- [39] J. Klein, *Polym. Adv. Technol.* **2012**, 23, 729.
- [40] R. Jayasekara, I. Harding, I. Bowater, G. B. Y. Christie, G. T. Lonergan, *Polym. Test.* **2004**, 23, 17.
- [41] T. Yamaoka, Y. Tabata, Y. Ikada, *J. Pharm. Pharmacol.* **1995**, 47, 479.
- [42] A. Besheer, K. Maeder, S. Kaiser, J. Kressler, C. Weis, E. K. Odermatt, *J. Biomed. Mater. Res., Part B* **2007**, 82, 383.
- [43] W. D. Comper, L. M. Hilliard, D. J. Nikolic-Paterson, L. M. Russo, *Am. J. Physiol. Renal Physiol.* **2008**, 295, F1589.
- [44] Y. Jiang, et al., *J. Biomed. Mater. Res., Part B* **2010**, 93, 275.
- [45] A. Schädlich, T. Naolou, E. Amado, R. Schöps, J. Kressler, K. Mäder, *Biomacromolecules* **2011**, 12, 3674.
- [46] Y. Kaneo, S. Hashihama, A. Kakinoki, T. Tanaka, T. Nakano, Y. Ikeda, *Drug Metab. Pharmacokinet.* **2005**, 20, 435.
- [47] P. Dahiya, R. Kamal, *N. Am. J. Med. Sci* **2013**, 5, 309.
- [48] L. Shi, X. Liu, W. Wang, L. Jiang, S. Wang, *Adv. Mater.* **2019**, 31, 1804187.
- [49] R. A. Clark, *The Molecular and Cellular Biology of Wound Repair*, New York: Plenum Press **1996**, pp. 3–33.
- [50] C. J. Wilson, R. E. Clegg, D. I. Leavesley, M. J. Pearcy, *Tissue Eng.* **2005**, 11, 1.
- [51] L. Anderson, N. G. Anderson, *Proc. Natl. Acad. Sci. USA* **1977**, 74, 5421.
- [52] R. R. R. Janeiro, Y. Zhu, T. Chen, S. Li, *Tissue Eng., Part A* **2014**, 20, 285.
- [53] J. Song, T. M. Lutz, N. Lang, O. Lieleg, *Adv. Healthcare Mater.* **2020**, 10, 2000831.
- [54] T. Crouzier, H. Jang, J. Ahn, R. Stocker, K. Ribbeck, *Biomacromolecules* **2013**, 14, 3010.
- [55] W. Kafenhah, J. D. Buttle, D. Burnett, P. A. Hollander, *Biochem. J.* **1998**, 330, 897.
- [56] G.-A. Junter, P. Thébault, L. Lebrun, *Acta Biomater.* **2016**, 30, 13.
- [57] G. A. Carlson, J. L. Drago, B. Samimi, D. A. Bruckner, G. W. Bernard, M. Hedrick, P. Benhaim, *Biochem. Biophys. Res. Commun.* **2004**, 321, 472.
- [58] J. E. Rayahin, J. S. Buhrman, Y. Zhang, T. J. Koh, R. A. Gemeinhart, *ACS Biomater. Sci. Eng.* **2015**, 1, 481.
- [59] B. Saleh, H. K. Dhaliwal, R. Portillo-Lara, E. Shirzaei Sani, R. Abdi, M. M. Amiji, N. Annabi, *Small* **2019**, 15, 1902232.
- [60] Z. Li, K. M. Bratlie, *Macromol. Biosci.* **2021**, 21, 2100031.
- [61] H. Yan, M. Hjorth, B. Winkeljann, I. Dobryden, O. Lieleg, T. Crouzier, *ACS Appl. Mater. Interfaces* **2020**, 12, 19324.
- [62] E. Nyman, J. Henricson, B. Ghafouri, C. D. Anderson, G. Kratz, *Plast. Reconstr. Surg. Global Open* **2019**, 7, 2221.
- [63] M. G. Neuman, R. M. Nanau, L. Oruña-Sanchez, G. Coto, *J. Pharm. Pharm. Sci.* **2015**, 18, 53.
- [64] A. Fallacara, S. Vertuani, G. Panozzo, A. Pecorelli, G. Valacchi, S. Manfredini, *Molecules* **2017**, 22, 2104.
- [65] Y. Ma, J. Yao, Q. Liu, T. Han, J. Zhao, X. Ma, Y. Tong, G. Jin, K. Qu, B. Li, F. Xu, *Adv. Funct. Mater.* **2020**, 30, 2001820.
- [66] B. Xu, A. Li, R. Wang, J. Zhang, Y. Ding, D. Pan, Z. Shen, *Adv. Funct. Mater.* **2021**, 31, 2105265.
- [67] Z. Ni, H. Yu, L. Wang, X. Liu, D. Shen, X. Chen, J. Liu, N. Wang, Y. Huang, Y. Sheng, *Adv. Healthcare Mater.* **2022**, 11, 2101421.
- [68] N. Pandey, A. Hakamivala, C. Xu, P. Hariharan, B. Radionov, Z. Huang, J. Liao, L. Tang, P. Zimmern, K. T. Nguyen, Y. Hong, *Adv. Healthcare Mater.* **2018**, 7, 1701069.
- [69] L. Han, M. Wang, P. Li, D. Gan, L. Yan, J. Xu, K. Wang, L. Fang, C. W. Chan, H. Zhang, H. Yuan, X. Lu, *ACS Appl. Mater. Interfaces* **2018**, 10, 28015.
- [70] H.-J. Park, Y. Jin, J. Shin, K. Yang, C. Lee, H. S. Yang, S.-W. Cho, *Biomacromolecules* **2016**, 17, 1939.
- [71] H. Jung, M. K. Kim, J. Y. Lee, S. W. Choi, J. Kim, *Adv. Funct. Mater.* **2020**, 30, 2004407.
- [72] D. Zhou, S. Li, M. Pei, H. Yang, S. Gu, Y. Tao, D. Ye, Y. Zhou, W. Xu, P. Xiao, *ACS Appl. Mater. Interfaces* **2020**, 12, 18225.
- [73] X. Fan, Y. Fang, W. Zhou, L. Yan, Y. Xu, H. Zhu, H. Liu, *Mater. Horiz.* **2021**, 8, 997.
- [74] K. Boettcher, B. Winkeljann, T. A. Schmidt, O. Lieleg, *Biotribology* **2017**, 12, 43.
- [75] C. A. Rickert, B. Wittmann, R. Fromme, O. Lieleg, *ACS Appl. Mater. Interfaces* **2020**, 12, 28024.
- [76] C. Kimna, B. Winkeljann, J. Song, O. Lieleg, *Adv. Mater. Interfaces* **2020**, 7, 2000735.

- [77] J. Shin, J. S. Lee, C. Lee, H.-J. Park, K. Yang, Y. Jin, J. H. Ryu, K. S. Hong, S.-H. Moon, H.-M. Chung, H. S. Yang, S. H. Um, J.-W. Oh, D.-I. Kim, H. Lee, S.-W. Cho, *Adv. Funct. Mater.* **2015**, *25*, 3814.
- [78] B. Winkeljann, A. B. Bussmann, M. G. Bauer, O. Lieleg, *Biotribology* **2018**, *14*, 11.
- [79] S. H. Tan, N.-T. Nguyen, Y. C. Chua, T. G. Kang, *Biomechanics* **2010**, *4*, 032204.
- [80] D. T. Eddington, J. P. Puccinelli, D. J. Beebe, *Sens. Actuators, B* **2006**, *114*, 170.
- [81] S. Raymentl, G. Liul, *J. Dent. Res.* **2000**, *79*, 1765.